



This is a repository copy of *A targeted search for binary white dwarf pulsars using Gaia and WISE*.

White Rose Research Online URL for this paper:
<https://eprints.whiterose.ac.uk/id/eprint/226781/>

Version: Published Version

Article:

Pelisoli, I. orcid.org/0000-0003-4615-6556, Marsh, T.R. orcid.org/0000-0002-2498-7589, Tovmassian, G. orcid.org/0000-0002-2953-7528 et al. (24 more authors) (2025) A targeted search for binary white dwarf pulsars using Gaia and WISE. *Monthly Notices of the Royal Astronomical Society*, 540 (1). staf761. ISSN 0035-8711

<https://doi.org/10.1093/mnras/staf761>

Reuse

This article is distributed under the terms of the Creative Commons Attribution (CC BY) licence. This licence allows you to distribute, remix, tweak, and build upon the work, even commercially, as long as you credit the authors for the original work. More information and the full terms of the licence here:
<https://creativecommons.org/licenses/>

Takedown

If you consider content in White Rose Research Online to be in breach of UK law, please notify us by emailing eprints@whiterose.ac.uk including the URL of the record and the reason for the withdrawal request.



eprints@whiterose.ac.uk
<https://eprints.whiterose.ac.uk/>

A targeted search for binary white dwarf pulsars using *Gaia* and WISE

Ingrid Pelisoli ¹★, T. R. Marsh ¹, G. Tovmassian ², L. A. Amaral ³, Amornrat Aungwerojwit ⁴, M. J. Green ⁵, R. P. Ashley ⁶, David A. H. Buckley ^{7,8,9}, B. T. Gänsicke ¹, F.-J. Hamsch ^{10,11,12}, K. Inight ¹, S. B. Potter ^{7,13}, A. J. Brown ¹⁴, N. Castro Segura ¹, V. S. Dhillon ^{15,16}, M. J. Dyer ¹⁵, J. A. Garbutt ¹⁵, D. Jarvis ¹⁵, M. R. Kennedy ¹⁷, S. O. Kepler ¹⁸, P. Kerry ¹⁵, S. P. Littlefair ¹⁵, J. McCormac ¹, J. Munday ¹, S. G. Parsons ¹⁵, E. Pike ¹⁵ and D. I. Sahman ¹⁵

¹Department of Physics, University of Warwick, Gibbet Hill Road, Coventry CV4 7AL, UK

²Instituto de Astronomía, Universidad Nacional Autónoma de México, Aptdo Postal 106, Ensenada 22860, Baja California, México

³Instituto de Física y Astronomía, Universidad de Valparaíso, Gran Bretaña 1111, Playa Ancha, Valparaíso 2360102, Chile

⁴Department of Physics, Faculty of Science, Naresuan University, Phitsanulok 65000, Thailand

⁵Max-Planck-Institut für Astronomie, Königstuhl 17, D-69117 Heidelberg, Germany

⁶Astrophysics Research Institute, Liverpool John Moores University, 146 Brownlow Hill, L3 5RF Merseyside, UK

⁷South African Astronomical Observatory, PO Box 9, Observatory, 7935 Cape Town, South Africa

⁸Department of Astronomy, University of Cape Town, Private Bag X3, Rondebosch 7701, South Africa

⁹Department of Physics, University of the Free State, PO Box 339, Bloemfontein 9300, South Africa

¹⁰Vereniging Voor Sterrenkunde (VVS), Zeeweg 96, B-8200 Brugge, Belgium

¹¹Bundesdeutsche Arbeitsgemeinschaft für Veränderliche Sterne (BAV), Munsterdamm 90, D-12169 Berlin, Germany

¹²American Association of Variable Star Observers, Cambridge, MA 02138, USA

¹³Department of Physics, University of Johannesburg, PO Box 524, Auckland Park 2006, South Africa

¹⁴Hamburger Sternwarte, University of Hamburg, Gojenbergsweg 112, D-21029 Hamburg, Germany

¹⁵Astrophysics Research Cluster, School of Mathematical and Physical Sciences, University of Sheffield, Sheffield S3 7RH, UK

¹⁶Instituto de Astrofísica de Canarias, E-38205 La Laguna, Tenerife, Spain

¹⁷School of Physics, University College Cork, Cork T12 K8AF, Ireland

¹⁸Instituto de Física, Universidade Federal do Rio Grande do Sul, 91501-970 Porto Alegre, RS, Brazil

Accepted 2025 May 6. Received 2025 May 6; in original form 2025 March 31

ABSTRACT

After its discovery in 2016, the white dwarf binary AR Scorpii (AR Sco) remained for several years the only white dwarf system to show pulsed radio emission associated with a fast-spinning white dwarf. The evolutionary origin and the emission mechanism for AR Sco are not completely understood, with different models proposed. Testing and improving these models requires observational input. Here, we report the results of a targeted search for other binary white dwarf pulsars like AR Sco. Using data from *Gaia* and the Wide-field Infrared Survey Explorer (WISE), we identified 56 candidate systems with similar properties to AR Sco, of which 26 were previously uncharacterized. These were subject to spectroscopic and photometric follow-up observations. Aside from one new binary white dwarf pulsar found, J191213.72–441045.1, which was reported in a separate work, we find no other systems whose characteristics are akin to AR Sco. The newly characterized systems are primarily young stellar objects (with 10 found) or cataclysmic variables (7 identifications), with the remaining being either blended or non-variable on short time-scales.

Key words: novae, cataclysmic variables – stars: pre-main-sequence – stars: variables: general – stars: variables: T Tauri, Herbig Ae/Be – white dwarfs.

1 INTRODUCTION

Non-thermal emission from stars is a sign of relativistic particle acceleration in the presence of magnetic fields. Most commonly detected from pulsars and black hole jet sources, the discovery of AR Scorpii (henceforth AR Sco) showed that white dwarfs can also generate substantial levels of non-thermal flux (Marsh et al. 2016). AR Sco is a binary system composed of a rapidly spinning,

magnetic white dwarf and a low-mass main-sequence star of M-type. Its most striking characteristic is pulsed emission that is detected from radio (Stanway et al. 2018) to X-rays (Takata et al. 2018) on a period of 1.97 min. Although radio emission has been detected in accreting white dwarfs (e.g. Coppejans et al. 2015; Barrett et al. 2020; Ridder et al. 2023) and from the two so-called magnetic propellers (Bookbinder & Lamb 1987; Pretorius et al. 2021), where material is being transferred but is ejected before accretion on to the white dwarf, AR Sco was the first white dwarf showing radio pulses in the absence of mass transfer, which led to it becoming known as a white dwarf pulsar.

* E-mail: ingrid.pelisoli@warwick.ac.uk

Similar to neutron star pulsars, the pulsed luminosity of AR Sco is powered by the rapid spin-down of the white dwarf ($P/\dot{P} \sim 5 \times 10^6$ yr, Stiller et al. 2018; Gaibor et al. 2020; Pelisoli et al. 2022), and its broad-band spectral energy distribution is consistent with synchrotron emission from relativistic electrons. However, in the case of AR Sco, binary interaction seems to be the main driver of the emission.¹ The emission is most likely triggered by the injection of particles into the magnetosphere of the white dwarf as it sweeps past the cool companion (Geng, Zhang & Huang 2016; Potter & Buckley 2018), but the exact mechanism behind the pulses is not fully understood.

The rapid spin-down of AR Sco suggests that it could be an evolutionary link between the two main classes of accreting magnetic white dwarfs, polars (also known as AM Her stars, Cropper 1990) and intermediate polars (IPs or DQ Her stars, Patterson 1994). In polars, the white dwarf spin is synchronized with the orbital period of the binary, whereas in IPs the white dwarf spin period is faster than the orbital period. A model for this possible evolutionary link has been proposed by Schreiber et al. (2021). They proposed that accreting magnetic white dwarfs are originally not strongly magnetic, which allows them to accrete efficiently from the companion, gaining angular momentum that causes spin-up. As the white dwarf cools, the core starts to crystallize, which, combined with the fast rotation, potentially creates the conditions for a dynamo (Isern et al. 2017; Ginzburg et al. 2022). Once a magnetic field emerges, the observed system is an accreting magnetic white dwarf spinning faster than the orbit – an IP. When the white dwarf’s magnetic field becomes strong enough, it will connect with the magnetic field of the M-dwarf, providing a synchronizing torque that causes the white dwarf to spin-down and transfers angular momentum from its spin to the orbit. That may cause the system to become detached, and be observed as a binary white dwarf pulsar, with a fast spin-down and no accretion, like AR Sco. Over time, the white dwarf spin will synchronize with the orbit, and angular momentum loss due to magnetic braking and gravitational wave radiation will bring the stars closer together again, mass transfer restarts, and the system thus becomes a polar.

The models for AR Sco’s pulsed emission, as well as the model for its formation, require observational input to be tested. In particular, there is still uncertainty as to whether a crystallization dynamo is possible for white dwarfs (e.g. Fuentes et al. 2023). One of the predictions of Schreiber et al. (2021)’s evolutionary model is that binary white dwarf pulsars are a possible evolutionary stage in the evolution of accreting white dwarfs, suggesting that binary white dwarf pulsars should be a class of systems. The discovery of J191213.72–441045.1 (J1912–4410, Pelisoli et al. 2023; Schwöpe et al. 2023) provides support for this hypothesis, although it is unclear whether J1912–4410 fits the crystallization model given the white dwarf’s estimated physical parameters (Pelisoli et al. 2024a). A potential connection between these systems and long-period radio transients, some of which have been found to harbour white dwarf binaries (de Ruiter et al. 2025; Hurley-Walker et al. 2024; Rodriguez 2025), is another avenue that requires further investigation that would benefit from a larger sample of binary white dwarf pulsars allowing a better picture of the characteristics of this class.

Arguably one of the reasons why so few binary white dwarf pulsars are known is the lack of systematic searches for similar systems. AR Sco itself was misclassified as a δ -Scuti variable for decades (Satyvaldiev 1971) before its then unique nature was discovered by

¹For this reason, we refer to AR Sco as a *binary* white dwarf pulsar throughout this work.

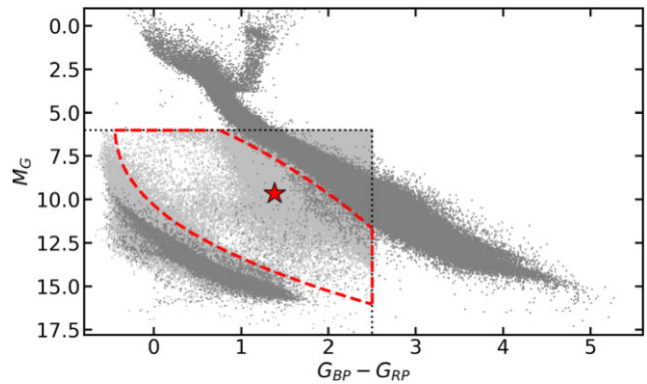


Figure 1. The first step in the candidate selection, using *Gaia* only. The red star shows the position of AR Sco. Our initial selection is marked by the black dotted lines. The lower M_G limit was defined to exclude hot subdwarf stars, and the upper $G_{BP} - G_{RP}$ limit aims at excluding low-mass main sequence stars and brown dwarfs. The objects initially selected are shown in light grey, whereas in dark grey we show the population within 100 pc to illustrate the location of main sequence and of the white dwarf cooling track. The red dashed lines show the final *Gaia* selection, excluding single white dwarfs and main-sequence stars.

citizen astronomers. A possible exception is the recent search for radio emission from white dwarfs using data from the Very Large Array Sky Survey (VLASS) Epoch 1 Quick Look Catalogue (Gordon et al. 2020, 2021) carried out by Pelisoli et al. (2024b). However, this search utilized a white dwarf catalogue (Gentile Fusillo et al. 2021) whose selection criteria are tailored for isolated white dwarfs and in fact exclude AR Sco. The search uncovered no secure radio detection from a white dwarf above the VLASS threshold (1–3 mJy), with only one white dwarf system possibly having associated radio emission, though other observational evidence favours a chance alignment. Their main conclusion was that strong radio emission from white dwarfs must be rare outside of interacting binaries, therefore an efficient selection for white dwarf pulsars needs to take binarity into account. In this work, we take that into consideration and report the results of a systematic search for binary white dwarf pulsars. We selected candidates showing similar observational properties to AR Sco and carried out follow-up observations to characterize them.

2 CANDIDATE SELECTION

2.1 *Gaia* eDR3

Given its nature as a binary system containing a white dwarf and a cool main-sequence star, AR Sco sits in a low-density region in the *Gaia* colour–magnitude diagram, as shown in Fig. 1. Therefore, the first step in our candidate selection was to identify sources in the same region of this diagram as AR Sco. We initially selected objects in a broad region defined by:

$$G_{BP} - G_{RP} < 2.5, \quad (1)$$

$$M_G > 6, \quad (2)$$

where G_{BP} and G_{RP} are the apparent magnitudes in the *Gaia* BP and RP passbands, and M_G is the absolute magnitude in the *Gaia* G passband, initially calculated without any parallax zero-point correction, that is $5 + 5 \log(\varpi/1000) + G$, where ϖ is the reported parallax. It is worth noting that, even though our selection was applied using eDR3 data, astrometric and photometric measurements are the same in DR3 as in eDR3.

In addition, to avoid the selection of systems with bad astrometry or photometry, we limited the uncertainties in parallax and in observed fluxes using:

$$\varpi/\sigma_\varpi > 10, \quad (3)$$

$$F_{BP}/\sigma_{F_{BP}} > 9, \quad (4)$$

$$F_{RP}/\sigma_{F_{RP}} > 9, \quad (5)$$

where σ_ϖ is the parallax uncertainty, and $F_{BP/RP}$ and $\sigma_{F_{BP/RP}}$ are the reported fluxes and flux uncertainties in the BP/RP passbands. The limits were tailored to recover AR Sco, which despite its brightness shows relatively high F_{BP} uncertainty due to variability ($F_{BP}/\sigma_{F_{BP}} = 9.943569$).

We also applied similar quality control criteria as in Pelisoli & Vos (2019), which were designed to exclude systems with bad parallax without removing known close binaries, namely:

$$E < 1.45 + 0.06(G_{BP} - G_{RP})^2, \quad (6)$$

$$E > 1.0 + 0.015(G_{BP} - G_{RP})^2, \quad (7)$$

$$u < 1.2 \max(1, \exp(-0.2(G - 19.5))), \quad (8)$$

where E is the excess noise when the G band is compared to $G_{BP} + G_{RP}$ ($\text{phot_bp_rp_excess_noise}$), and $u = \sqrt{\text{astrometric_chi2_al}/(\text{astrometric_n_good_obs_al} - 5)}$, with $\text{astrometric_chi2_al}$ and $\text{astrometric_n_good_obs_al}$ being, respectively, the value of the chi-square statistic of the astrometric solution and the number of good observations. The expression \max indicates that u is compared with 1.2 times the largest value between 1 or $\exp(-0.2(G - 19.5))$.

This initial selection resulted in 28 124 276 objects, as illustrated in Fig. 1. Next, we selected objects lying between the main sequence and the white dwarf cooling track, like AR Sco. We applied the following selection:

$$M'_G < 5.25 + 7((G_{BP} - G_{RP}) + 0.45)^{2/5}, \quad (9)$$

$$M'_G > 4.45 - 5.15(1 - \exp(0.35(G_{BP} - G_{RP}))) \quad (10)$$

which is also shown in Fig. 1. Here, we applied the median zero-point parallax of -0.017 mas to calculate M'_G (Lindegren et al. 2021). These cuts were tailored to approximately fit the 0.99 percentiles for the main sequence and for white dwarfs, thus excluding the vast majority of these systems from the selection. This *Gaia* selection resulted in 181 171 objects.

2.2 WISE

Another remarkable characteristic of AR Sco is its infrared variability. Most white dwarfs are too faint in the infrared to be detected as variables, and therefore infrared variability can be a good initial identifier for binary white dwarf pulsars. To identify variable candidates, we matched the *Gaia* selection using a 5 arcsec radius with data from both the original (cryogenic) Wide-field Infrared Survey Explorer mission (WISE; Wright et al. 2010) and from AllWISE (Cutri et al. 2021), which combines the cryogenic and post-cryogenic (NEOWISE, Mainzer et al. 2011) survey phases. Both these catalogues contain variable flags that are 4-digit strings, with each digit corresponding to one of the WISE bands (W_1 , W_2 , W_3 , and W_4 , which are centred at 3.4, 4.6, 12, and 22 μm , respectively). The value of each digit goes from 0 to 9 (with n for insufficient or

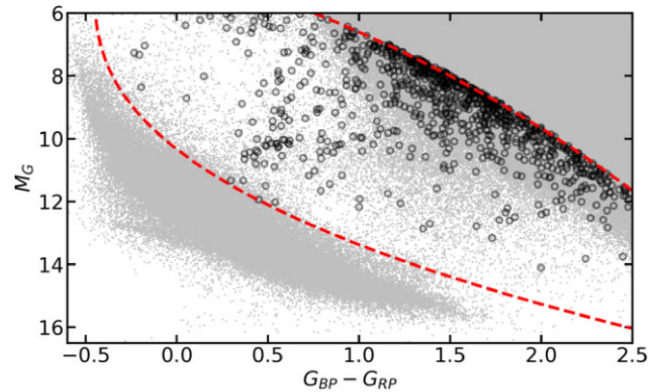


Figure 2. *Gaia* colour–magnitude diagram showing as black circles the 844 sources within our selected ranges (red dashed lines) flagged as variable. The grey points are the sources passing the initial colour–magnitude and quality selection (equations 1–8).

inadequate data); the higher the number, the larger the probability of variability in a given band. Values of 5 or lower can generally be regarded as non-variable sources, 6–7 are potentially low amplitude variables, and 8–9 are likely variables. For AR Sco, the flags are 9999 for WISE and 8866 for AllWISE. We selected as possible variables all objects whose flags contained a digit equal to or higher than 7. The angular resolution of WISE is, however, relatively poor (6–12 arcsec), making contamination by nearby sources common, which can lead to erroneous variability identification. Contamination is also flagged in both WISE and AllWISE with a four-digit string, similarly to the variability. A zero indicates no contamination, and different letters are used to indicate possible sources of contamination (for AR Sco, the flags are 0000 in both WISE and AllWISE). We flagged as possibly contaminated all objects whose contamination flag contained h/H, p/P, d/D, or o/O in either WISE or AllWISE. These indicate, respectively, potential contamination or spurious detection due to halo, persistent image, diffraction spikes, or optical ghosts caused by nearby stars. In this way, we identified 731 uncontaminated potential variable sources in WISE and 185 in AllWISE (with 102 common to both). We also flagged as variable objects those classified as variable in Petrosky et al. (2021) which had no contaminated flag (213 sources, 30 not flagged as variable in WISE or AllWISE). We therefore identified 844 candidate variables among the systems selected from *Gaia*, shown in Fig. 2.

Finally, AR Sco’s emission contains a significant contribution from non-thermal sources, unlike most systems lying on the same region of the *Gaia* colour–magnitude diagram, which we expect to be primarily detached white dwarf-main sequence binaries. We identified the WISE colour $W_1 - W_2$ as a good proxy for this, as AR Sco clearly stands out from the bulk of other systems selected from *Gaia*, as shown in Fig. 3. Taking this into account, we applied a colour cut requiring either the WISE or the AllWISE value $W_1 - W_2$ to be larger than 0.5 to the variable sources, which resulted in 56 candidates, as well as recovering AR Sco itself. All of the steps in the candidate selection are summarized in Table 1.

3 LITERATURE AND ARCHIVAL DATA

The 56 candidate binary white dwarf pulsars are listed in Table 2. 30 of these systems are known and previously well characterized as other types of sources in the literature. These are briefly discussed in Section 3.1. The other systems were not known or not well characterized, that is, they are only mentioned as candidates or

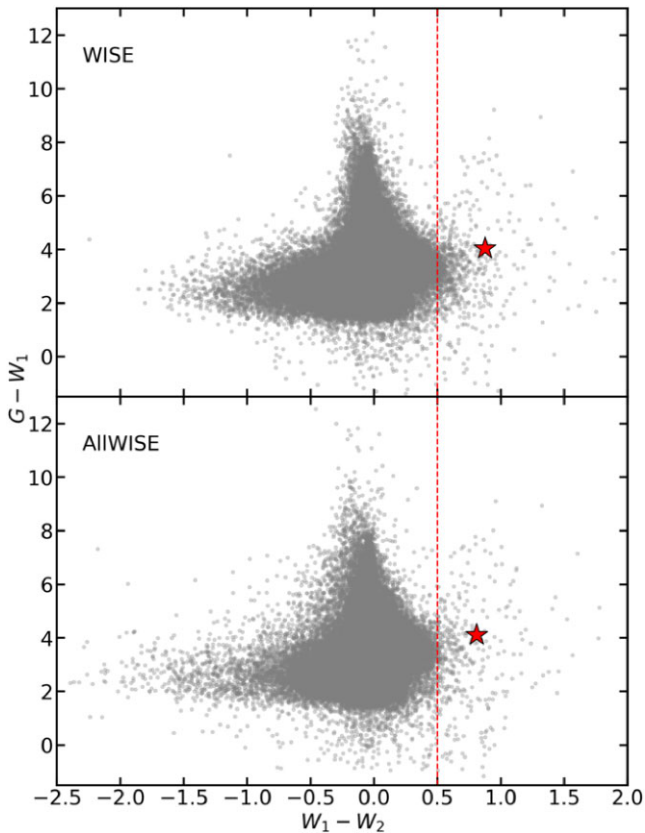


Figure 3. Colour–colour diagrams showing *Gaia* $G - W_1$ versus $W_1 - W_2$ for objects in the *Gaia* selection that have WISE (top) or AllWISE (bottom) data. The red star shows the location of AR Sco, which motivated the selection $W_1 - W_2 > 0.5$ (red dashed line).

detections. We first assessed the available archival data for these systems, as described in Section 3.2.

3.1 Known systems

Out of the 56 candidates identified in our initial search, 13 are known polars that have previously been well-characterized in the literature. All but one have orbital periods shorter than 3 h. One system is an intermediate polar with spin and orbital periods of 23 and 81 min, respectively. Finally, 16 objects are characterized as young stellar objects (YSOs), such as T Tauri stars. This large contamination likely arose due to our use of infrared variability as a criterion, which is also a characteristic of YSOs still surrounded by the remnants of the star-forming cloud. Notes and references on these 30 previously characterized systems are given in Appendix A and their classes are given in Table 2.

3.2 Analysis of available archival data

The remaining 26 objects were not previously characterized in the literature, or had existing inconclusive characterization. We first analysed archival photometric data that could potentially reveal pulses as those shown by AR Sco. Specifically, we analysed data from the *Transiting Exoplanet Survey Satellite* (*TESS*; Ricker et al. 2015), the Zwicky Transient Facility (ZTF; Bellm et al. 2019), the Asteroid Terrestrial-impact Last Alert System (ATLAS; Tonry et al. 2018), and the Catalina Real-Time Transient Survey (CRTS; Drake

et al. 2009). The availability of data and the conclusions drawn from each data set are summarized in Table 3.

3.3 TESS

The *TESS* mission monitored more than 85 per cent of the sky. Each sector – a pre-defined $24^\circ \times 90^\circ$ region of the sky – is monitored for 27 d consecutively, with a brief interruption halfway through for data downlinking. There is overlap between different sectors, such that the total baseline can be as long as 351 continuous days (for stars around the ecliptic poles). The cadence of available light curves is either 20 s or 2 min, and 10 min or 30 min images are available for all observed sectors. The pixel size is 21 arcmin, meaning that contamination from nearby stars is a potential issue.

No 20-sec light curves were available for the 26 uncharacterized objects. Three out of the 26 objects (J0354+1652, J0408+6046, and J1828+2823) have available 2-min light curves. We used specifically the light curves provided by the *TESS* Science Processing Operations Center and the PDCSAP flux, which corrects an initial simple aperture photometry (SAP) to remove instrumental trends and contributions from neighbouring stars other than the target of interest using a pre-search data conditioning (PDC). All but five systems have 10/30-min images. We performed the photometry for these images using ELEANOR (Feinstein et al. 2019) in a custom-built script.²

Out of the 21 targets with available data, eight show clear periodic variability (see Fig. 4), with an additional system potentially showing a periodicity on top of stochastic behaviour (Fig. 5). The obtained periods range from 1.3 to over 50 h. Performing pre-whitening revealed no independent periods – all other periodicities could be attributed to harmonics or cadence aliases. Given the periods and light curve shapes, the most probable causes for variability are binarity (irradiation or eclipses) or rotation; no pulsing behaviour like that of AR Sco is seen in the light curves. Three systems (J0452+3017, J0428+3300, and J1912+4410) display saw-tooth-shape light curves with periods of the order of hours, similar to the orbital behaviour shown by AR Sco. J1912+4410 was later confirmed as a binary white dwarf pulsar from follow-up observations (Pelisoli et al. 2023; Schwöpe et al. 2023b).

Three other systems also show aperiodic variability, as shown in Fig. 6. Our adopted criterion for aperiodic variability is the same used by Pelisoli et al. (2024b), where the distribution of standard deviations from the mean is compared with the maximum expected deviation from the mean given the number of observations. Gaussian noise is assumed to calculate the maximum expected deviation, and a threshold of more than 10 per cent of the observations above the expected deviation (to allow for systematics) is used to define variability. The cause for aperiodic variability could be, for example, changes in accretion rate in systems that have a disc, such as cataclysmic variables (CVs) and YSOs. The other nine systems show no detectable periodic or aperiodic variability.

3.4 ZTF

ZTF uses the 1.2-m Palomar telescope to monitor the northern sky (declination $\gtrsim -25^\circ$). The exposure time is 30 sec and observations use primarily the g and r filters, with occasional observations in the i band. Images are usually taken every three nights, with some fields

²<https://github.com/ipelisoli/eleanor-LS>

Table 1. Summary of the stages in our candidate selection.

Total number of sources in Gaia eDR3	1811 709 771
Sources after quality and initial colour–magnitude cuts (equations 1–8)	28 124 276
Objects within the final colour–magnitude selection (equations 9–10)	181 171
Systems showing WISE variability	844
Candidates with $W_1 - W_2 > 0.5$	56

Table 2. The 56 binary white dwarf pulsar candidates in our selection. Columns are the *Gaia* DR3 source identification, the Simbad ID (if the source has been previously well characterized), right ascension (RA) and declination (Dec) in J2000, and the *Gaia* apparent DR3 *G* magnitude. We also include the GALEX *NUV* magnitude when available, and the X-ray observatory that reported a detection. These two columns were not used in the candidate selection, but defined follow-up priority. Magnitudes are truncated reflecting precision. We also define a short name for each object which is used throughout the paper for simplicity. The last column indicates the classification of each system, preceded by * if it was determined as part of this work, as detailed in the text.

source_id	Simbad primary ID	RA	Dec	<i>G</i>	<i>NUV</i>	X-ray	Short name	Type
4702994514879977472		00:07:43.23	−69:59:47.7	19.153	17.726	<i>ROSAT</i>	J0007−6959	*Polar
4697621824327141248	V* BL Hyi	01:41:00.40	−67:53:27.5	17.2134	17.657	<i>XMM-NEWTON</i>	J0141−6753	Polar
4617143036371460864		01:56:37.23	−83:58:34.2	16.697	17.260	<i>ROSAT</i>	J0156−8358	*CV
5093945085525624448	SSS J035055.8−204817	03:50:55.99	−20:48:15.8	14.775	17.627		J0350−2048	YSO
5107845936158224768		03:54:10.31	−16:52:50.0	17.346	18.048	<i>ROSAT</i>	J0354−1652	*CV
3302990624137350528	CRTS J035758.7+102943	03:57:58.66	+10:29:42.4	18.102		<i>XMM-NEWTON</i>	J0357+1029	Polar
473695898746498560		04:08:21.86	+60:46:49.1	15.553	19.64		J0408+6046	*YSO
4871949697851411456		04:28:11.54	−33:00:01.4	18.182	18.89		J0428−3300	*Polar
4628229751415342976		04:35:09.62	−75:27:44.0	16.912	17.424	<i>ROSAT</i>	J0435−7527	*Polar
159891122647000192		04:52:54.56	+30:17:19.0	18.524	21.32		J0452+3017	*IP
4877265084954805504	PPMXL 2431202680279124324	05:03:49.25	−28:23:08.3	17.731	17.876	<i>XMM-NEWTON</i>	J0503−2823	IP
3223542525253775104	2MASS J05301240+0148214	05:30:12.40	+01:48:21.4	16.612			J0530+0148	YSO
4798833587650467200	V* UW Pic	05:31:35.65	−46:24:05.0	15.861	18.099	<i>XMM-NEWTON</i>	J0531−4624	Polar
3223900068396361856	2MASS J05315396+0242310	05:31:53.96	+02:42:31.2	17.742			J0531+0242	YSO
3016473390180542720	2MASS J05371640−0711463	05:37:16.41	−07:11:46.4	17.481			J0537−0711	YSO
3334578455035280128		05:39:03.52	+08:24:24.3	18.563			J0539+0824	*YSO
3216423702860032896	2MASS J05405519−0247497	05:40:55.19	−02:47:49.8	17.466			J0540−0247	YSO
3336335474617325568	Gaia DR2 3336335474617325568	05:41:07.12	+09:18:43.4	17.353			J0541+0918	YSO
3216159442110928256	2MASS J05422602−0308566	05:42:26.03	−03:08:56.8	17.077			J0542−0308	YSO
3335057979544055168		05:51:28.99	+07:52:41.0	17.808			J0551+0752	*YSO
3100846613967311232		06:57:15.12	−06:15:42.6	16.745			J0657−0615	*YSO
3116059834803771904	PPMXL 3189652360374206258	07:06:48.92	+03:24:47.3	17.134		<i>XMM-NEWTON</i>	J0706+0324	Polar
1101817445394854400	V* HS Cam	07:19:14.52	+65:57:44.3	18.784	18.48	<i>XMM-NEWTON</i>	J0719+6557	Polar
5532757148220186880		07:59:32.31	−44:12:25.2	18.123			J0759−4412	*YSO
3038572263932589696		08:08:06.87	−09:35:13.6	18.4041			J0808−0935	Unclear
5719598950133755392	V* VV Pup	08:15:06.80	−19:03:17.8	15.955		<i>XMM-NEWTON</i>	J0815−1903	Polar
5329108769930689664	Gaia DR2 5329108769930689664	08:42:45.77	−48:11:42.0	17.873			J0842−4811	YSO
790222752096510592		11:25:44.34	+50:12:18.0	18.7939	18.743		J1125+5012	Unclear
5788603818854455680	[FLG2003] eps Cha 11	12:01:43.47	−78:35:47.2	17.111			J1201−7835	YSO
3513017956589117056		12:26:37.90	−23:04:14.5	19.536	22.97		J1226−2304	Unclear
6086028036361965952		13:01:56.68	−47:02:05.4	15.315			J1301−4702	*YSO
6067533838480626432		13:05:47.97	−55:02:34.0	16.249			J1305−5502	*YSO
3718095055765579136	BPS CS 30311−0012	13:25:22.38	+06:00:28.8	14.538	18.75		J1325+0600	YSO
6096905573613586944	V* V834 Cen	14:09:07.29	−45:17:16.0	16.609		<i>XMM-NEWTON</i>	J1409−4517	Polar
5846719394999359232		14:25:40.45	−68:37:32.9	18.406			J1425−6837	*CV
5893562752219619200	2MASS J14534105−5521387	14:53:41.06	−55:21:38.7	15.214		<i>INTEGRAL</i>	J1453−5521	Polar
6243210920137332096	CRTS J155929.1−223618	15:59:29.21	−22:36:17.5	16.937			J1559−2236	YSO
6243223873758073728	EPIC 204388640	16:02:04.30	−22:31:46.9	17.209			J1602−2231	YSO
6242434969863194880	2MASS J16063093−2258150	16:06:30.92	−22:58:15.1	18.475			J1606−2258	YSO
6048855674228736128	Gaia DR2 6048855674228736128	16:17:44.78	−25:09:15.5	17.882			J1617−2509	YSO
6033663795136741888		16:57:52.61	−26:31:52.6	17.6845			J1657−2631	Unclear
4476137370261520000	V* V2301 Oph	18:00:35.53	+08:10:13.9	16.605	17.540	<i>XMM-NEWTON</i>	J1800+0810	Polar
4585783762161656832		18:28:29.47	+28:23:46.0	15.489	18.25		J1828+2823	*YSO
4273036059117893632	2MASS J18294021+0015127	18:29:40.22	+00:15:13.0	18.384			J1829+0015	YSO
4079708070610098432		18:45:53.17	−21:46:34.9	17.644			J1845−2146	Unclear
2262055164796424576	V* EP Dra	19:07:06.19	+69:08:43.9	18.046	17.969	<i>XMM-NEWTON</i>	J1907+6908	Polar
6712706405280342784		19:12:13.72	−44:10:45.1	17.094	18.411		J1912−4410	Pulsar
4186053835982000512		19:17:16.07	−12:31:16.7	15.894	19.38		J1917−1231	*YSO
6640165468504197120	2MASS J19293303−5603434	19:29:33.04	−56:03:43.0	17.328			J1929−5603	Polar
6909026160627539840		20:59:52.90	−07:47:13.9	19.1572			J2059−0747	Unclear
6883251168530612352		21:01:24.67	−16:16:07.5	18.7265			J2101−1616	Unclear
6827850007422236928		21:19:12.62	−23:08:09.1	18.6381			J2119−2308	Unclear
2222486906706076544	2MASS J21205785+6848183	21:20:57.85	+68:48:18.4	17.018			J2120+6848	YSO
1956566510538468224	Gaia DR2 1956566510538468224	22:04:50.69	+40:08:38.4	18.498	19.79	<i>ROSAT</i>	J2204+4008	Polar
1777232423131443840	RX J2218.5+1925	22:18:32.76	+19:25:20.5	17.312	18.053	<i>XMM-NEWTON</i>	J2218+1925	Polar
1925212909978565632		23:36:11.32	+44:25:39.6	16.907			J2336+4425	*YSO

Downloaded from https://academic.oup.com/mnras/article/540/1/821/8127238 by University of Sheffield user on 27 May 2025

Table 3. Summary of the analysis of archival photometric data for the 26 uncharacterized systems. Columns are the short name defined in Table 2, and the drawn conclusion (periodic, variable with no significant period, or not observed to vary – NOV) based on *TESS*, *ZTF*, *ATLAS*, and *CRTS* is listed. For periodic systems, we also give the period from the dominant peak in hours. When the periodicity was found in more than one data set, we report the period from *TESS* which was more precise in all cases. Periods from different surveys were always consistent.

Short name	<i>TESS</i>	<i>ZTF</i>	<i>ATLAS</i>	<i>CRTS</i>	Period (h)
J0007–6959	Periodic	No data	Variable	No data	1.5826 ± 0.0040
J0156–8358	Periodic	No data	Variable	No data	2.348 ± 0.035
J0354–1652	Periodic	Periodic	Periodic	Aperiodic	1.690 ± 0.034
J0408+6046	NOV	Variable	Periodic?	No data	1.71 ± 0.14
J0428–3300	Periodic	No data	Variable	NOV	2.5466 ± 0.0011
J0435–7527	Periodic	No data	Periodic	Variable	2.36 ± 0.23
J0452+3017	Periodic	Periodic	Periodic	No data	1.325 ± 0.008
J0539+0824	NOV	Variable	Variable	Variable	–
J0551+0752	NOV	Variable	Variable	Variable	–
J0657–0615	Variable	Variable	Variable	No data	–
J0759–4412	NOV	No data	Variable	No data	–
J0808–0935	NOV	NOV	NOV	No data	–
J1125+5012	NOV	Variable	Variable	No data	–
J1226–2304	NOV	NOV	NOV	NOV	–
J1301–4702	Periodic?	No data	Variable	Variable	54 ± 7
J1305–5502	Periodic	No data	Variable	No data	35.2 ± 0.9
J1425–6837	NOV	No data	Variable	No data	–
J1657–2631	No data	NOV	NOV	No data	–
J1828+2823	Variable	Variable	Variable	No data	–
J1845–2146	No data	NOV	NOV	No data	–
J1912–4410	Periodic	No data	Periodic	Variable	4.037 ± 0.006
J1917–1231	No data	Variable	Variable	No data	–
J2059–0747	No data	NOV	NOV	No data	–
J2101–1616	No data	NOV	NOV	NOV	–
J2119–2308	NOV	NOV	NOV	NOV	–
J2336+4425	Variable	Variable	Variable	Variable	–

observed for longer in ‘deep drilling’ events. Photometry is made available through the NASA/IPAC Infrared Science Archive.

17 out of the 26 uncharacterized systems have *ZTF* data. All of these have *r* band data and all but one (J1125+5012) have *g* data. Six have *i* band data, but only one of these (J1125+5012, the same system that has no *g* data) has a substantial number of measurements (>100). To search for periodic signals, we calculated a multiband periodogram as described by VanderPlas & Ivezić (2015) using *gatspy* (Vanderplas 2015), which implements a weighted sum of individual Lomb–Scargle periodograms. We used the *g* and *r* data, except in the case of J1125+5012 where *r* and *i* were used. Two systems (J0354–1652 and J0452+3017) were found to show periodic behaviour with periods consistent with those found in the *TESS* data. Like previously, pre-whitening revealed no additional periodicities. It is worth noting that none of the other systems found to be periodic with *TESS* have *ZTF* data. Eight systems are aperiodic according to the metric described previously; four of these appeared to be constant in *TESS* – possibly because of flux dilution from nearby stars, or due to longer term variability than the *TESS* baseline – and one had no *TESS* data. These five systems whose variability had not been revealed by *TESS* are shown in Fig. 7. Seven systems showed no detectable periodic or aperiodic variability.

3.5 ATLAS

ATLAS utilizes four 0.5-m telescopes (two in Hawaii, one in Chile, one in South Africa) to scan the sky, primarily to detect Near Earth Objects. The exposures are 30-sec long and use broad orange (*o*) and cyan (*c*) filters. The whole sky is scanned down to a magnitude of about 19.5 with a cadence of one day for declinations between -50 and $+50^\circ$ or two days in the polar regions. To obtain

photometric measurements for the 26 systems, we employed the forced photometry server.³

We analyse the data in the same way as the *ZTF* data, by doing a multiband periodogram and by searching for aperiodic variability. We find five systems showing detectable periodic variability, four of which show periods consistent with those found by *TESS* and a fifth that was not detected as periodic by *TESS* or *ZTF* (though aperiodic variability was seen in *ZTF*). The light curve for this system is shown in Fig. 8. The periodogram is dominated by one-day aliases, but an independent periodicity can also be seen. Additionally, two systems found to be constant with *TESS* and that had no *ZTF* data appear to be variable in *ATLAS*. They are shown in Fig. 9. Results for other systems are consistent with the *TESS* and *ZTF* findings, that is periodic systems were found to be variable even if the period was undetermined, and systems appearing constant in *TESS* and *ZTF* were also found to be constant in *ATLAS*.

3.6 CRTS

CRTS uses three telescopes, two in the northern hemisphere (the 0.7-m Catalina Sky Survey telescope at Mt. Bigelow Station, and the 1.5-m Mt. Lemmon Survey telescope) and one in the southern hemisphere (the 0.5-m Siding Springs Survey telescope, which was discontinued in 2013). No filters are used, but magnitudes are made available in an approximate *V* scale. Typically four 30-sec exposures are obtained per night, reaching a limiting magnitude around 19–21.

CRTS data are available for 11 out of the 26 uncharacterized objects. No new variables are revealed by this data set. Seven

³<https://fallingstar-data.com/forcedphot/>

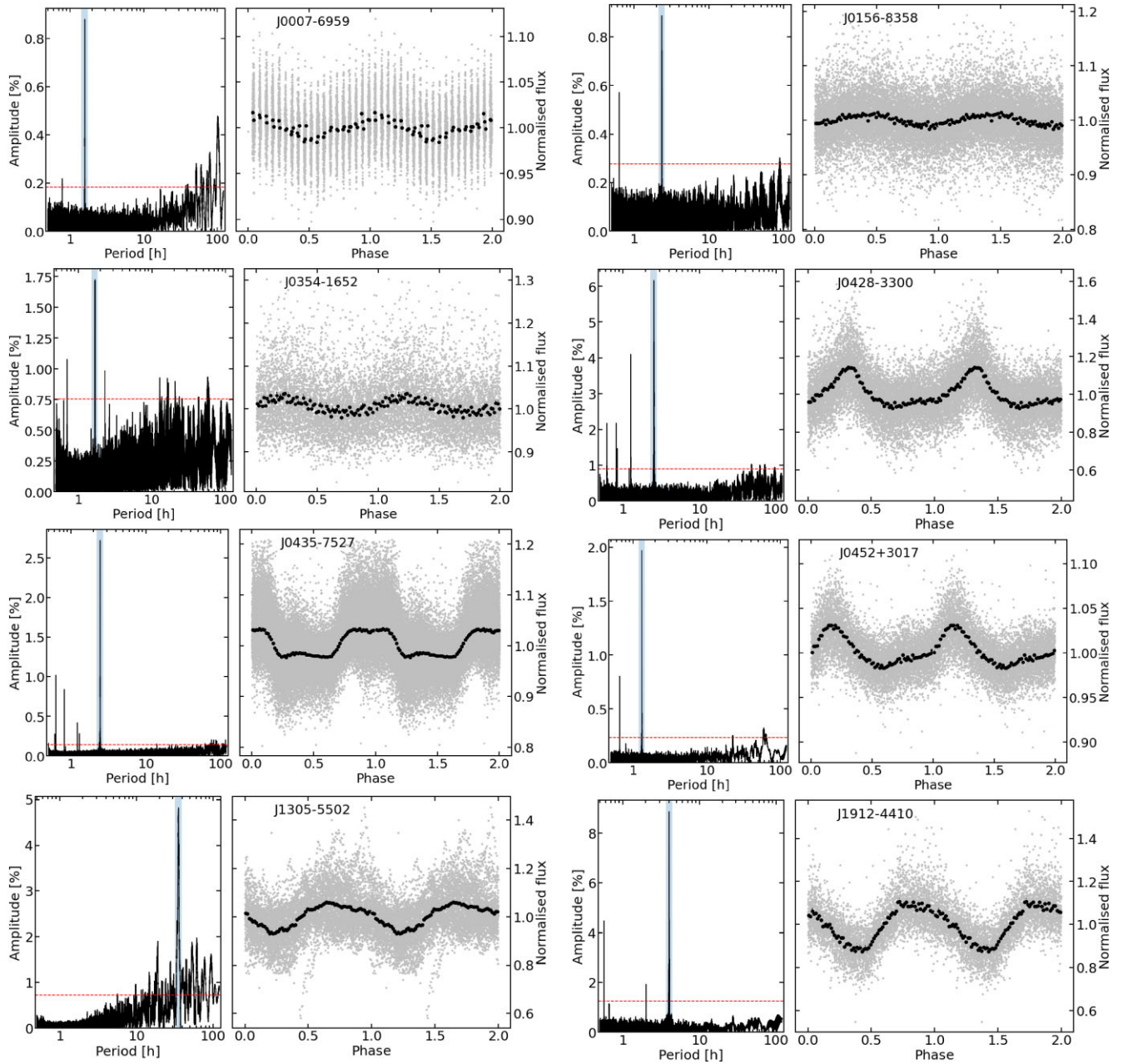


Figure 4. The eight systems showing periodic variability in *TESS* data. In each case, the left panel shows the periodogram, with the horizontal red dashed line indicating an average 5σ detection limit. The blue shaded area indicates the dominant period, with the data folded to that period showed on the right panels in grey dots. The black filled circles show the data averaged to 100 phase bins (the zero-point of phase was arbitrary at this stage).

systems met our criterion for aperiodic variability (all of which were also found to vary with other surveys), whereas the remaining four systems showed no detectable variability.

4 FOLLOW-UP OBSERVATIONS AND ANALYSIS

4.1 High-speed time-series photometry

The cadence and exposure time of photometric surveys is not ideal for identifying fast pulsed variability like that seen for AR Sco on a 2-min time-scale. Therefore, most of the 26 uncharacterized systems were also followed up with the high-speed photometers ULTRACAM (Dhillon et al. 2007) and ULTRASPEC (Dhillon et al.

2014). ULTRACAM is mounted on the 3.5-m European Southern Observatory (ESO) New Technology Telescope and is equipped with a beam splitter that allows simultaneous observations in three filters. ULTRASPEC is installed on the 2.4-m Thai National Telescope and observes only one band at a time. In both cases, the readout time is negligible ($\lesssim 0.5$ ms) thanks to frame-transfer capabilities. The journal of observations is detailed in Table 4. All data were reduced using the HiPERCAM pipeline.⁴ We carried out bias subtraction, flat-field correction, and then aperture photometry using a constant

⁴<https://cygnus.astro.warwick.ac.uk/phsaap/hipercam/docs/html/>

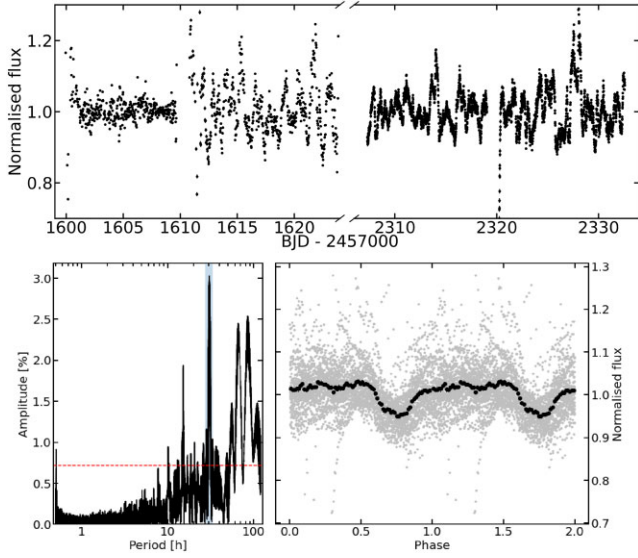


Figure 5. J1301–4702, which shows both aperiodic variability (clear in the top panel) and potential periodic variability as suggested in the bottom panels (left is the periodogram, right the phase folded light curve). The potential period (indicated by the blue shading) is above a 1 per cent false alarm probability calculated by randomizing the flux measurements and recalculating the periodogram.

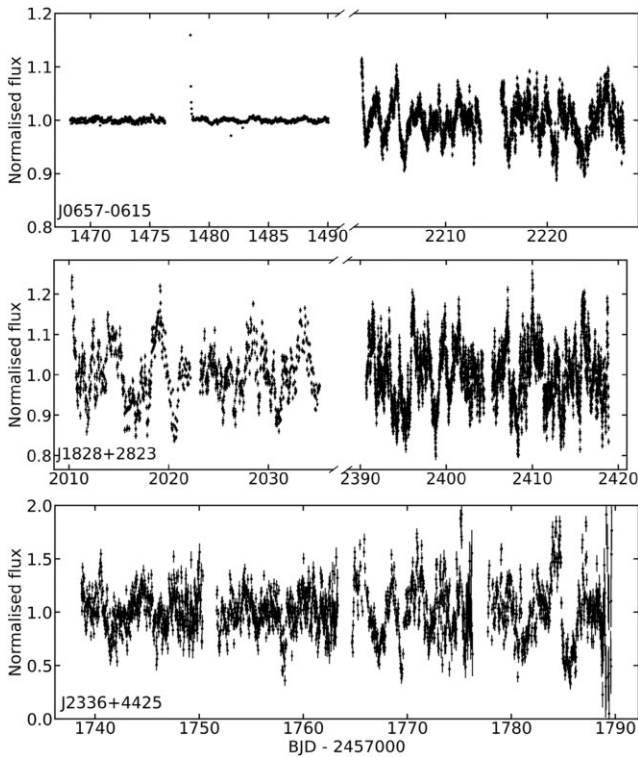


Figure 6. Light curves for the three systems showing aperiodic variability in *TESS* data. The big change in amplitude for J0657–0615 could be due to a change in state between the two observations; however, given the large pixel size of *TESS*, the change could also be explained by a change in the contribution from other sources to the aperture.

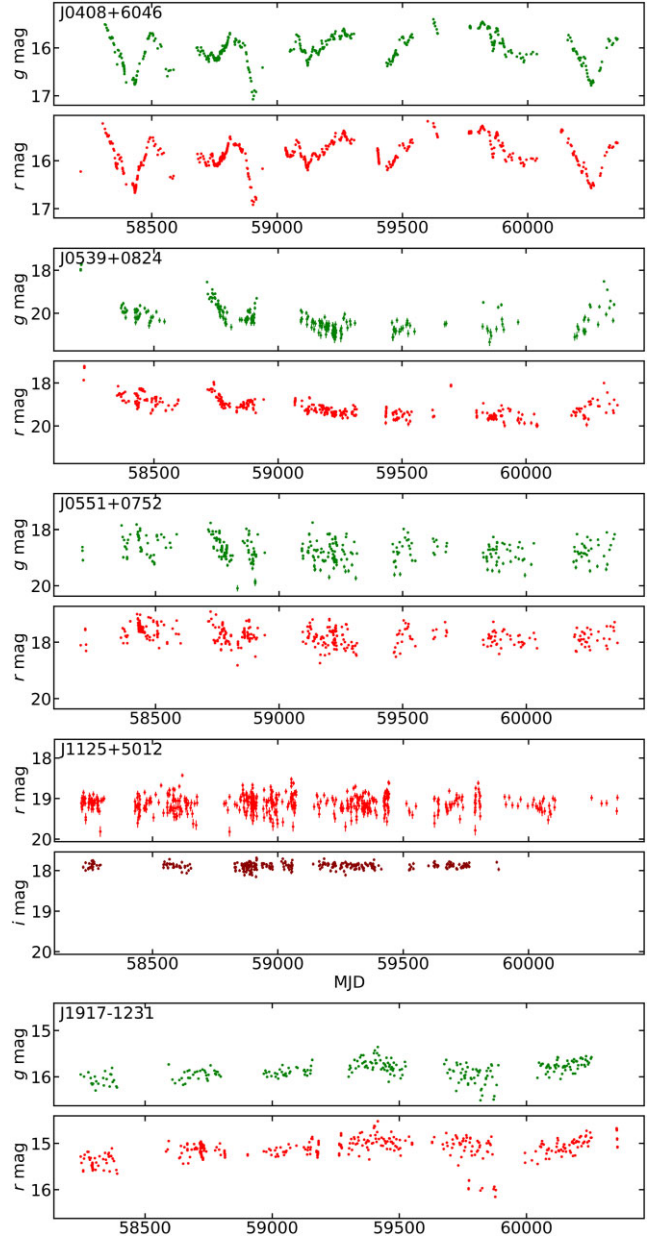


Figure 7. Light curves for the five systems that show aperiodic variability in ZTF.

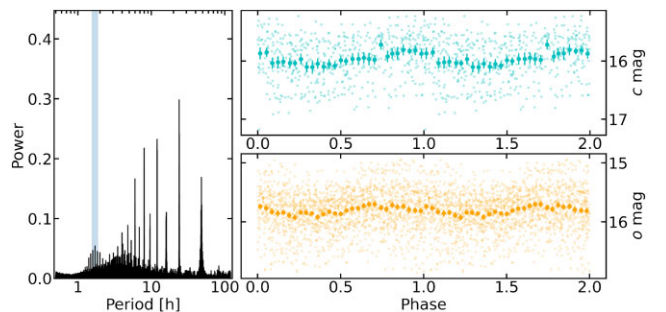


Figure 8. J0408+6046, the system showing periodic variability detected only with *ATLAS*. The left panel shows the periodogram which is dominated by one-day aliases; the possible period is marked by the shaded blue region. The *c* (top) and *o* (bottom) light curves folded to this period are shown on the right panels.

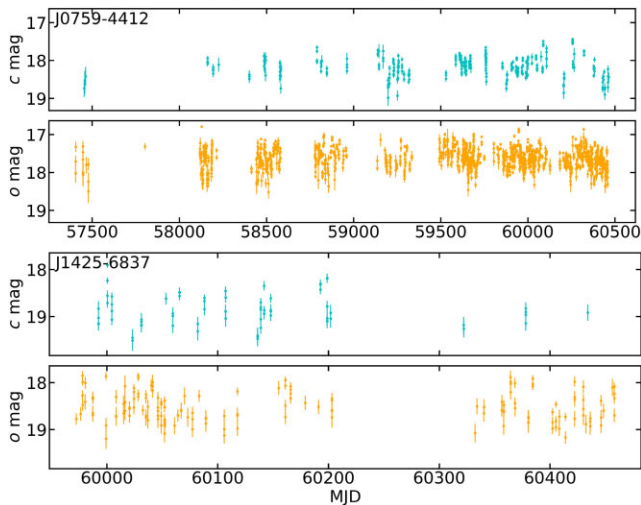


Figure 9. Light curves for the two systems showing aperiodic variability not detected in *TESS* but detected in *ATLAS*.

star as reference. The same star was used when observations were repeated in more than one night.

Six systems showed fast and seemingly stochastic variability in their light curves, typical of CV systems. For two of these, J0156–8358 and J0354–1652, Fourier analysis revealed no periodic variability (see Fig. 10). J0428–3300 and J0435–7527 show potential quasi-periodic oscillations (QPOs), whose frequency drifts and sometimes is not even detected. For J0428–3300 that translates to a periodogram peak at 3.676 ± 0.009 min, and for J0435–7527 there is a peak 4.24 ± 0.11 min (see Fig. 11). J1425–6837, was constant and barely detectable in two observations, and then detected and stochastically variable the next year, suggesting it might be a dwarf nova (see Fig. 12) with the abrupt brightness change caused by a sudden dumping of matter on to the white dwarf due to instability in the disc (e.g. Hameury 2020). Finally, J0452+3017 showed a hint of a period at 3.0 ± 0.5 min with visible pulsing behaviour (see Fig. 13), akin to AR Sco albeit with lower amplitude. This behaviour prompted dedicated time-resolved spectroscopy follow-up (Section 4.2.2).

Another six systems showed low-level variability and/or flaring, consistent with the behaviour of YSOs. These are shown in Fig. 14. The other nine systems observed with ULTRACAM/ULTRASPEC showed no detectable variability in the optical data. As they were selected based on infrared variability, the lack of optical variability might be because variability is concentrated in the infrared, or because the infrared variability is spurious due to background contamination.

4.2 Spectroscopy

Time-series photometry alone can be insufficient to provide a secure classification, as different types of systems can show similar variability characteristics. Therefore, we also strove to obtain spectroscopy for previously uncharacterized systems.

4.2.1 XSHOOTER at the VLT

The four previously uncharacterized systems that had reported X-ray detections (J0007–6759, J0156–8358, J0354–1652, J0435–7527) and additionally two systems showing UV detection and periodic variability in photometric surveys (J0428–3300, J1912–4410) were

observed with XSHOOTER at ESO’s 8.2-m Very Large Telescope (VLT; proposals 108.228J and 109.234F). Two spectra on consecutive nights were obtained for all targets (except J0428–3300, which was not observed a second time before the program was terminated) to probe for spectral variability and/or radial velocity changes. The spectra were automatically reduced by the XSHOOTER pipeline.

J1912–4410 showed a spectrum with a blue and a red component, with very narrow lines indicating absence of accretion, like seen for AR Sco, and its analysis was published in Pelisoli et al. (2023). The spectra for the other systems are shown in Fig. 15. All except J0156–8358 and J0354–1652 show strong He II emission (with strength comparable to the Balmer lines), which is a characteristic of magnetic systems with channelled accretion (e.g. Voikhanskaya 1987). J0007–6759, J0428–3300, and J0435–7527 show asymmetric line profiles that change from night to night (when more than one night was available). This suggests that they are polars – the asymmetry is caused by the combination of the narrow emission component from the bright spot with the broader emission from the accretion stream and irradiated companion. J0156–8358 and J0354–1652, on the other hand, show symmetric emission lines and are more likely non-magnetic CVs, given the weak He II emission.

4.2.2 OSIRIS at the GTC

Spectroscopic observations of J0452+3017 were performed with the 10.4 m Gran Telescopio Canarias (GTC) at the Observatorio del Roque de los Muchachos. The object was observed in service mode in a 2.5-h observing block on 2023 March 16, covering two cycles of the period detected in archival data. The spectra were taken with the Optical System for Imaging and low-intermediate-resolution Integrated Spectroscopy (OSIRIS) spectrograph (Cepa et al. 2003), which consists of a mosaic of two Marconi CCDs, each with 2048×4096 pixels. Each pixel has a physical size of $15 \mu\text{m}$. We used 1×1 binning for our observations, giving a plate scale of 0.127 arcsec. OSIRIS was used in long-slit mode, centring the object in CCD2. We used the R500R grism, providing 4800–10000 Å coverage at $R = 587$ resolution. 21 spectra of the object were obtained with 3600-sec exposure times, in dark, spectroscopic conditions with 1.3–1.4 arcsec seeing; the slit width was set to 1.0 arcsec. The data were reduced using IRAF to perform bias subtraction, flat-field correction and spectral extraction.

Fig. 16 shows the reduced co-added spectrum of J0452+3017 as well as the trailed spectra. The spectrum shows broad emission components, in particular $H\alpha$, whose radial velocity can be seen to vary periodically in the trail, a behaviour consistent with an IP. We estimated the radial velocity of the most prominent emission lines ($H\alpha$, He I 5875 Å, He II 5411 Å) by fitting Gaussian profiles with a fixed width (determined from the co-added spectrum) and variable centre. The radial velocities were fit to obtain the orbital ephemeris with the period fixed to the one derived from the *TESS* data (1.325 ± 0.008 h), as illustrated in Fig. 17. We obtained

$$\text{BJD(TDB)} = 2460020.43323(69) + 0.0552(3)E, \quad (11)$$

where BJD(TDB) is the barycentric Julian date in the Barycentric Dynamical Time (TDB) scale, and E is an integral cycle number. The obtained radial velocity amplitude was found to be $170.9 \pm 16.0 \text{ km s}^{-1}$, implying a binary mass function of $0.1029 \pm 0.0252 M_{\odot}$. The emission lines likely come from the irradiated surface of the companion and, as a consequence, the derived radial velocities are not those of the centre of mass of the companion. In fact, considerable scatter can be seen, suggesting that the different lines might

Table 4. Journal of ULTRACAM and ULTRASPEC observations with the object’s short name, the instrument used, filters, date the night started, the cadence and (in case of ULTRACAM) number of co-added u images, and the duration of the observation. J1912–4410 is omitted given that detailed ULTRACAM follow-up is described in Pelisoli et al. (2023).

source_id	Instrument	Filter(s)	Date	Cadence (s)	u co-adds	Duration (min)
J0007–6959	ULTRACAM	u, g, r	2024-05-03	7.0	3	35
J0156–8358	ULTRACAM	u, g, i	2022-03-06	3.0	3	38
J0354–1652	ULTRASPEC	g	2021-02-14	4.8	–	150
	ULTRASPEC	g	2021-02-15	4.8	–	104
	ULTRACAM	u, g, i	2021-03-07	2.5	3	108
J0428–3300	ULTRACAM	u, g, i	2021-03-10	6.0	3	49
	ULTRACAM	u, g, i	2021-03-17	3.1	3	131
	ULTRACAM	u, g, i	2021-07-08	5.0	3	81
	ULTRACAM	u, g, i	2021-11-08	3.0	4	173
J0435–7527	ULTRACAM	u, g, i	2021-01-22	5.8	3	98
	ULTRACAM	u, g, i	2021-03-08	5.8	3	175
J0452+3017	ULTRASPEC	g	2023-02-23	9.9	–	184
J0539+0824	ULTRACAM	u, g, r	2023-03-18	8.0	3	61
J0551+0752	ULTRACAM	u, g, i	2023-10-11	5.8	3	41
J0657–0615	ULTRASPEC	g	2022-02-07	4.9	–	61
	ULTRACAM	u, g, i	2023-03-09	4.0	3	106
J0759–4412	ULTRACAM	u, g, i	2023-03-12	6.5	3	16
	ULTRACAM	u, g, r	2023-03-19	4.0	3	69
	ULTRACAM	u, g, i	2023-03-29	3.4	3	84
J0808–0935	ULTRACAM	u, g, r	2023-04-23	5.1	3	31
J1226–2304	ULTRACAM	u, g, r	2023-04-23	8.1	5	47
	ULTRACAM	u, g, r	2024-02-09	5.7	3	103
J1301–4702	ULTRACAM	u, g, i	2021-03-09	1.0	4	70
	ULTRACAM	u, g, i	2021-03-10	2.4	2	46
J1305–5502	ULTRACAM	u, g, i	2022-06-05	8.0	3	94
J1425–6837	ULTRACAM	u, g, i	2022-06-06	9.0	3	39
	ULTRACAM	u, g, i	2022-06-07	5.1	3	24
	ULTRACAM	u, g, r	2023-04-23	8.1	3	110
	ULTRACAM	u, g, i	2023-04-29	5.0	3	36
J1657–2631	ULTRACAM	u, g, i	2022-06-07	4.1	5	32
	ULTRASPEC	KG5	2023-04-22	8.2	–	52
J1845–2146	ULTRACAM	u, g, r	2023-03-08	4.0	3	47
	ULTRACAM	u, g, i	2023-03-20	4.0	4	62
J1917–1231	ULTRACAM	u, g, i	2022-06-05	3.4	6	36
	ULTRASPEC	KG5	2023-04-22	3.1	–	41
J2059–0747	ULTRACAM	u, g, i	2023-10-17	6.1	3	64
J2101–1616	ULTRACAM	u, g, r	2023-04-23	5.8	5	61
	ULTRACAM	u, g, r	2023-10-18	5.8	3	31
J2119–2308	ULTRACAM	u, g, r	2023-09-14	5.8	3	28
J2336+4425	ULTRASPEC	g	2022-12-18	5.6	–	110

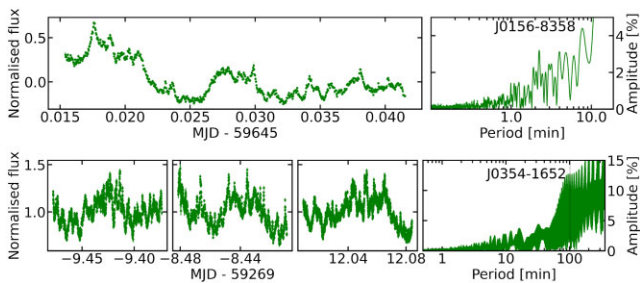


Figure 10. The g -band light curves (left panels) and periodogram (rightmost panel) for J0156–8358 (top) and J0354–1652 (bottom). No periods stand out from the background. The period detected in archival data for J0354–1652 is indicated by a vertical dashed line.

originate on different regions on the surface of the companion, depending on the temperature distribution. Therefore, the derived radial velocity amplitude and mass function are lower limits for this system.

4.3 Other instruments

J0408+6046 and J1828+2823 were observed with the Intermediate Dispersion Spectrograph (IDS) at the Isaac Newton Telescope (INT) as part of a search for CVs unrelated to this work. J0408+6046 was observed on three nights (2020 February 12, 2020 August 20, and 2020 December 17) and J1828+2823 on four nights (2020 May 15, 2020 September 10, 2020 September 12, and 2021 June 04), in all cases using the R632V grating. The spectra were reduced with PAMELA and MOLLY (Marsh 1989) and are shown in Fig. 18. J0408+6046 shows a spectrum typical of a pre-main sequence Herbig Ae star (Herbig 1960), with narrow Balmer lines and variable emission (most notably seen in $H\alpha$). J1828+2823 shows strong and narrow Balmer emission lines with no radial velocity variability, consistent with a YSO.

J1917–1231 was observed as backup target with FLOYDS during a follow-up survey of AM CVn systems. The pipeline-reduced spectra are shown in Fig. 19. Similar to J0408+6046, it shows features consistent with a Herbig Ae star.

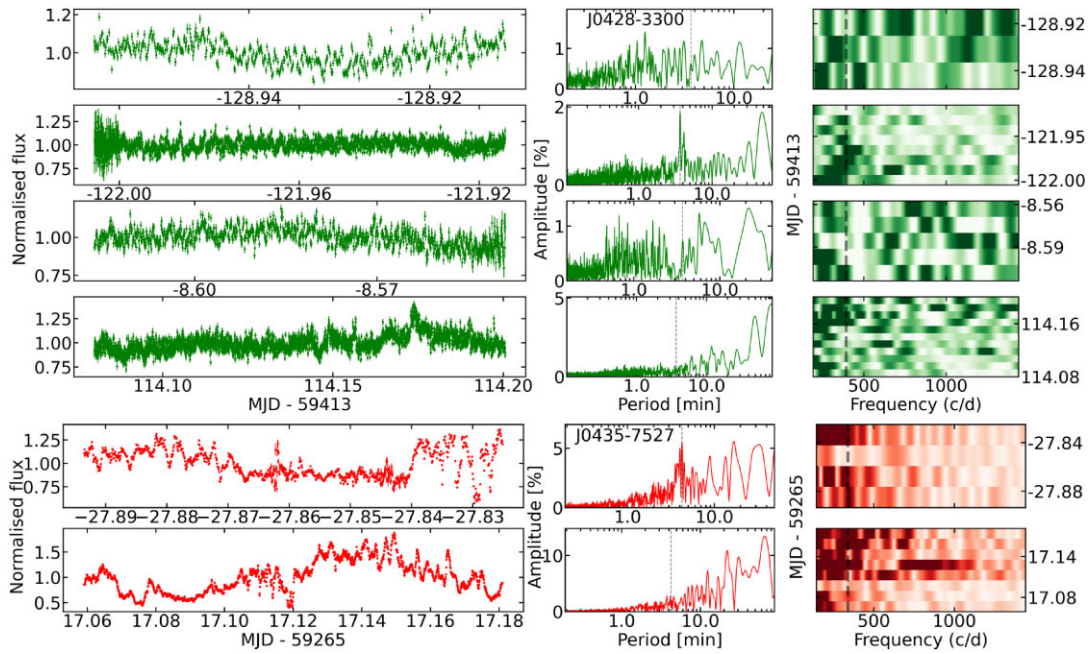


Figure 11. The light curves (left panels), periodogram (middle), and running Fourier transform (right) for the g data of J0428–3300 (top four panels, in green) and r data of J0435–7527 (bottom two panels, in red). Both systems show a peak in the periodogram (indicated by dashed vertical lines) that does not seem to be persistent, as it is not always detected and drifts in the running Fourier transform.

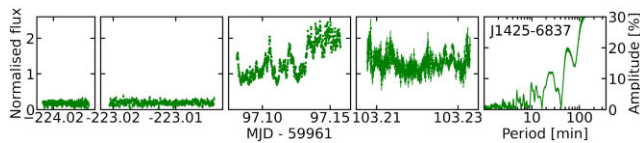


Figure 12. g -band light curves (left panels) and periodogram (rightmost panel, only including the two last nights of data) of J1425–6837. In the first two nights, the system has very low signal and was barely above the readout noise. The following year it was over a magnitude brighter and displaying variability.

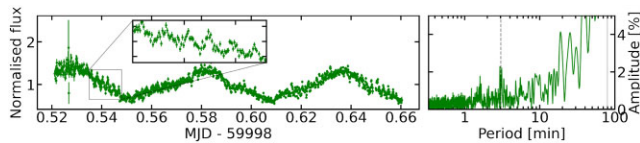


Figure 13. The g light curve of J0452+3017 (left panel), with an inset zooming in on the visible pulses. The right panel shows the periodogram with the newly detected period indicated by a vertical dashed line, and the period found with archival data shown by the solid grey line.

J1301–4702 and J1305–5502 were observed as backup targets with Goodman at SOAR using the 400 l/mm grating. Sixteen consecutive spectra were obtained for J1301–4702, covering a timespan of about 40 min. For J1305–5502, two consecutive spectra were obtained. The spectra were reduced with IRAF and are shown in Fig. 20. In both cases, narrow emission lines with no radial velocity variability are seen, suggesting these are also YSOs.

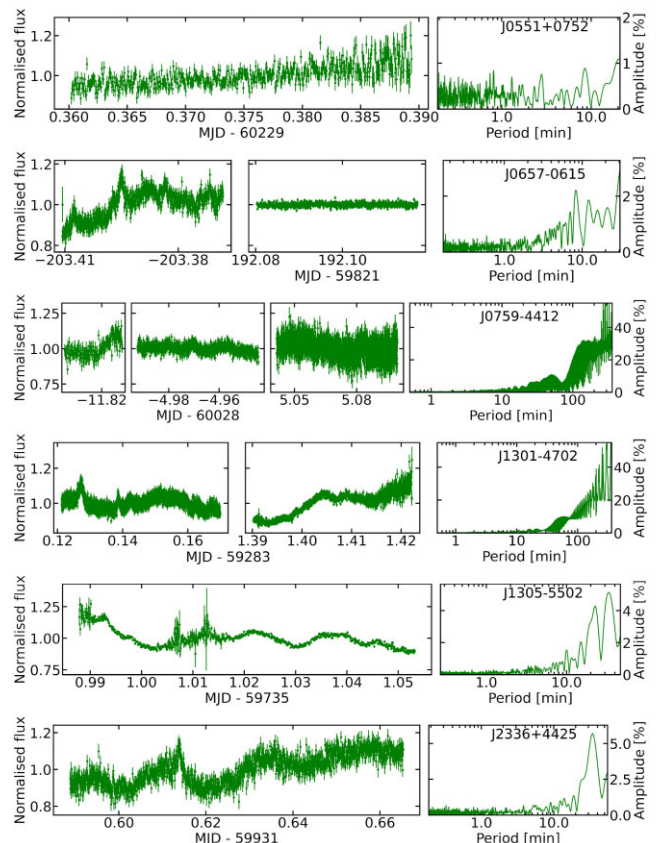


Figure 14. The g -band light curves (left panels) and periodogram (rightmost panel) for the six systems showing low-level aperiodic variability and flaring. For J0657–0615, which appeared constant on the second night, only the first night is included in the Fourier transform.

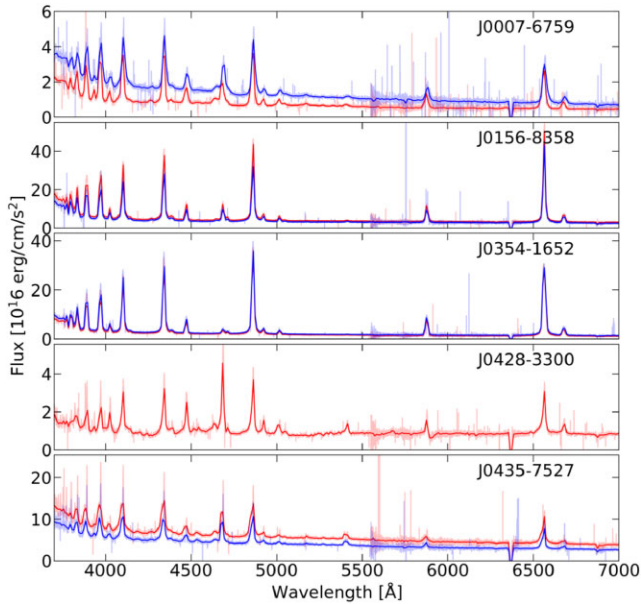


Figure 15. XSHOOTER spectra for J0007–6759, J0156–8358, J0354–1652, J0428–3300, and J0435–7527 (from top to bottom). The transparent lines show the actual spectra and the solid lines an average every 50 points. The first spectrum obtained is shown in red and the second (when available) in blue.

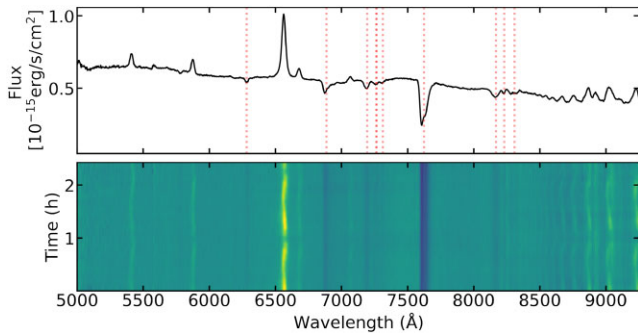


Figure 16. The top panel shows the co-added spectrum of J0452+3017 (telluric absorption lines are indicated by red dashed lines). The bottom panel shows the trailed spectra, which show that the radial velocity of the emission lines is changing periodically.

5 RESULTS AND DISCUSSION

5.1 Young stellar objects

Our follow-up observations suggest that ten out of the 26 previously uncharacterized objects are consistent with YSOs. J0408+6046 and J1917–1231 can be classified as Herbig Ae stars based on their spectra (Fig. 18, top and Fig. 19, respectively). Similarly, the narrow lines with no radial velocity variability seen for J1828+2823 (Fig. 18, bottom), J1301–4702 and J1305–5502 (both shown in Fig. 20) are consistent with T Tauri stars. Another system that is likely a YSO is J0539+0824, which showed variability with no determined period in archival data (Fig. 7), but no clear variability when observed with high-speed photometry, consistent with slow stochastic variability from a circumstellar disc. Additionally, it has been identified as potential member of a stellar association (Spina et al. 2021), which supports the interpretation as a YSO. J0551+0752, J0657–0615, J0759–4412, and J2336+4425 show a similar variability behaviour to J0539+0824, with only low-level variability and/or flaring (as

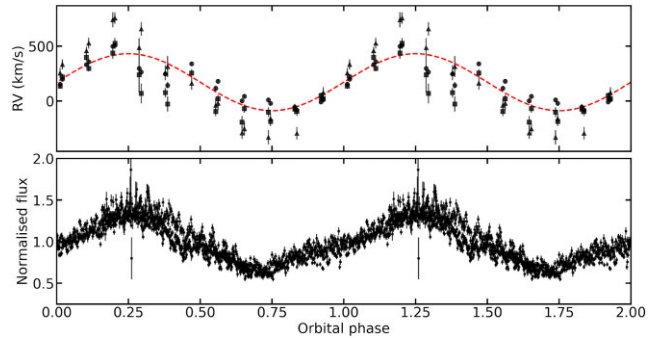


Figure 17. The radial velocities (top) and ULTRASPEC photometry (bottom) for J0452+3017 folded to the same orbital ephemeris given in equation (11). The red dashed line in the top panel shows the fit to the radial velocities.

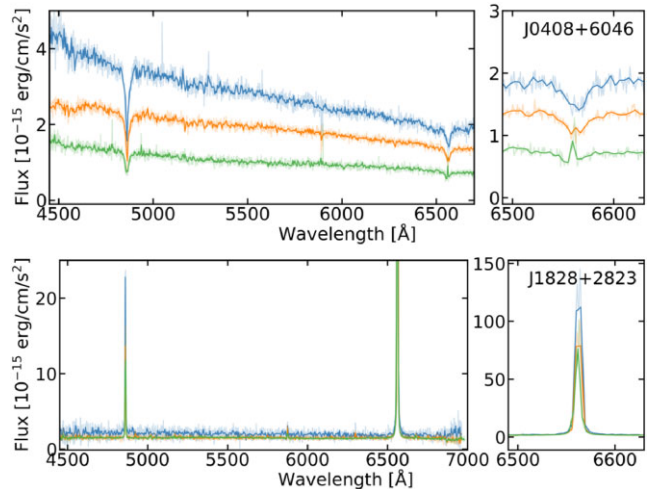


Figure 18. Spectra for J0408+6046 (top) and J1828+2823 (bottom) obtained with INT/IDS.

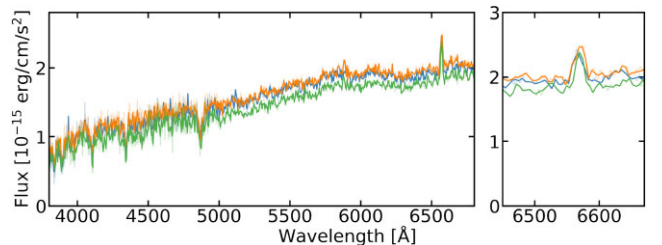


Figure 19. FLOYDS spectra of J1917–1231.

shown in Fig. 14), and thus our interpretation is that they are also YSOs.

Six out of these ten possible YSOs are in the catalogue of Marton et al. (2019), which used machine learning methods to identify YSO candidates from *Gaia* DR2 and WISE data. J0657–0615 appears as a high-probability (0.96) YSO, and is also classified as such by Wilson et al. (2023). J1305–5502 also has a moderately high YSO probability (0.85, when the WISE W3 and W4 bands are not included). The four other targets have a higher probability of being extragalactic objects according to their classification: J0408+6046 (0.64), J0539+0824 (0.98), J0551+0752 (0.79), and J0759–4412 (0.95). We can rule out an extragalactic origin for J0408+6046 based on its Herbig Ae-type spectrum, but the possibility of extragalactic origin remains open for the other three objects.

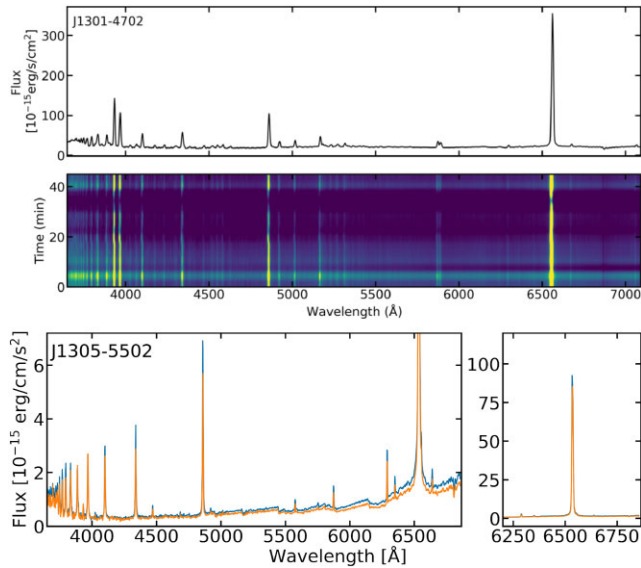


Figure 20. Co-added (top) and trailed (middle) spectra for J1301–4702 and the two spectra of J1305–5502, obtained with SOAR.

5.2 Polars

Three systems showed spectra (see Fig. 15) and light curves consistent with a polar: J0007–6959, J0428–3300, and J0435–7527. They are all newly discovered polars; J0007–6959 was classified as a white dwarf candidate by Gentile Fusillo et al. (2019). Curiously, J0435–7527 was classified as an RR Lyra based on its CRTS light curve (Drake et al. 2017). The orbital periods for these systems were determined from the *TESS* data (see Table 3 and Fig. 4) and are 1.5826 ± 0.0040 , 2.5466 ± 0.0011 , and 2.36 ± 0.23 h, placing two of them within the CV period gap between 2–3 h, believed to occur when the donor star becomes fully convective and magnetic braking becomes inefficient, giving the binary time to detach. This is in line with findings that polars do not actually show a period gap (e.g. Schreiber, Belloni & Schwöpe 2024).

J0428–3300 and J0435–7527 additionally show evidence for QPOs, as illustrated in Fig. 11. These are variations that show coherence over a limited amount of time and are a common feature of polars (e.g. Bera & Bhattacharya 2018), having been detected from infrared to X-rays. They generally group in two ranges of periods, a few (1–5) s or a few (4–10) min, with the latter being the most common feature in the optical (Potter et al. 2010). The QPOs observed for J0428–3300 and J0435–7527 at 3.676 ± 0.009 and 4.24 ± 0.11 min, respectively, are therefore consistent with a polar behaviour. The occurrence of QPOs, and other photometric variations seen at polars such as flickering, are believed to be caused by variations in the accretion flow, possibly due to inhomogeneities (Kuijpers & Pringle 1982), modulation at the edge of the white dwarf’s magnetosphere (Patterson, Williams & Hiltner 1981), or modulation near the L1 point due to irradiation (King 1989).

5.3 Intermediate polar

J0452+3017 showed an intermittent pulsing behaviour in its ULTRASPEC light curve with a period of 3.0 ± 0.5 min (Fig. 13), that prompted further follow-up. The obtained GTC spectra revealed broad and symmetric emission (Fig. 16) which, combined with the detection of a short spin period, suggest that this system is an intermediate polar. We have found its orbital period to be

1.325 ± 0.008 h, which makes it, to our knowledge, the intermediate polar with the shortest known orbital period.⁵

5.4 Likely non-magnetic CVs

The spectra of J0156–8358 and J0354–1652 (in Fig. 15) show only weak He II emission, suggesting they are non-magnetic CVs. Their light curves (Fig. 10), showing only stochastic variability on top of the orbital period – that is, with no clear detection of a spin period that could indicate an intermediate polar nature – support that conclusion. We put J1425–6837 in this category as well given the observed sudden change in brightness state (shown in Fig. 12), which is consistent with the behaviour of a dwarf nova, although some intermediate polars have been observed to show outbursts.

J0156–8358 appears in the literature only as an X-ray source, therefore its nature is determined for the first time here. Its orbital period is 2.348 ± 0.035 h, which interestingly places it in the period gap. The depth of this gap depends somewhat on the observed sample (see e.g. Inight et al. 2023), therefore finding systems within the gap is not completely unexpected; nevertheless, this makes this system a valuable addition to the CV population given the relative rareness of period-gap systems.

J0354–1652, on the other hand, was studied by Thorstensen, Lépine & Shara (2006) and more recently by Joshi et al. (2022). Thorstensen et al. (2006) found a hint of radial velocity variability at a period of 46 min and had no clear conclusions on the nature of the system, which is why we kept in our sample for further follow-up. Like Joshi et al. (2022), we found no indication of a 46 min period in the data. They report a likely orbital period of 1.689 ± 0.001 h, consistent with our findings. They similarly notice the weakness of He II as a sign of lack of magnetism, though they remark that the variability is akin to that seen in polars. We favour a non-magnetic classification based on the spectral features.

5.5 Other systems

J1125+5012 is in the vicinity (<7 arcsec) of a bright ($G = 13.2$) source, hence its photometry is likely contaminated by diffraction spikes from this neighbour. As a consequence, its selection as a candidate is unreliable and we pursued no follow-up, leaving its nature as undetermined.

Seven systems (J0808–0935, J1226–2304, J1657–2631, J1845–2146, J2059–0747, J2101–1616, and J2119–2308) showed no optical variability in either photometric surveys or high-speed follow-up, which ruled out a nature as binary white dwarf pulsars. Their nature is unclear based on existing data alone and we cannot rule out that the infrared variability that led to their selection is caused by background sources.

5.6 J191213.72–441045.1

The main discovery of this targeted search was J1912–4410, reported in detail in Pelisoli et al. (2023). It was selected as a candidate as its position in the *Gaia* colour–magnitude diagram, $W1 - W2$ colour (0.685) and WISE variability flag (999n) all fit the selection criteria. Subsequent follow-up found it to show pulsing behaviour in the optical with a period of 5.3 min, interpreted as the spin of the white dwarf. Pulses were also detected in the radio and in X-rays (Schwope et al. 2023). Like in AR Sco, the white dwarf has

⁵See <https://asd.gsfc.nasa.gov/Koji.Mukai/iphome/catalog/alpha.html>.

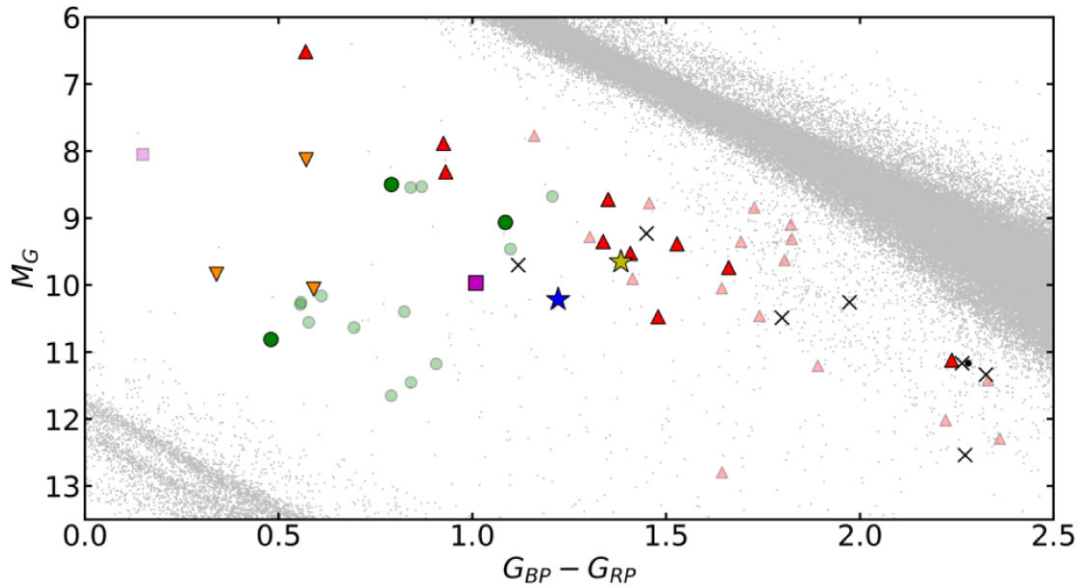


Figure 21. The location in the *Gaia* colour–magnitude diagram of the 56 binary white dwarf pulsar candidates. AR Sco is the yellow star and J1912–4410, discovered as a result of this work, is the blue star. Polars are shown as green circles, one IPs as a magenta squares, and red triangles are YSOs. The symbols are smaller and fainter for previously known objects. The orange upside-down triangles are the likely non-magnetic CVs, the black dot is the blended object that was not further followed up, and the black crosses showed no detectable variability in follow-up optical observations.

an M-type irradiated companion, and the orbital period determined from the *TESS* data (shown here in Fig. 4) is 4.03 h. The spectra of the system show narrow emission lines consistent with originating on the surface of the irradiated companion suggesting no persistent accretion, with the pulsed emission likely originating due to magnetic interaction between the two stars (Pelisoli et al. 2024a). All of these characteristics led to its classification as a second binary white dwarf pulsar.

6 SUMMARY AND CONCLUSIONS

We carried out a targeted search for binary white dwarf pulsars combining the astrometric and photometric data from *Gaia* with infrared data and variability flags from WISE. Based on criteria determined using the only previously known binary white dwarf pulsar, AR Sco, we identified 56 candidates (Table 2), 26 of which were previously uncharacterized systems. The remaining 30 were known in the literature and a mix of CVs and YSOs. We analysed archival times-series photometry for all previously unknown systems and carried out high-speed photometry and spectroscopy follow-up observations, prioritizing systems with detected variability.

We concluded that ten of the followed-up objects are YSOs, three are polars, one is an intermediate polar, and three are likely non-magnetic CVs. One system was not followed up due to blending, and seven systems showed no optical variability in either archival or follow-up light curves and were not further studied. Finally, one new binary white dwarf pulsar, J1912–4410, was identified. The location of these sources in the *Gaia* colour–magnitude diagram is shown in Fig. 21. The YSOs concentrate near the main sequence as expected, with the identified CVs (magnetic or otherwise) being located closer to the white dwarf cooling sequence. Like AR Sco, J1912–4410 is located somewhat between these two regions. A detailed characterization of this system was presented in a dedicated work (Pelisoli et al. 2023).

Although our search successfully identified one new binary white dwarf pulsar, that came at the expense of a large number of

contaminant sources, in particular YSOs. We believe that the YSO contamination is mainly driven by our use of infrared data, especially variability, as a criterion, given that YSOs are infrared bright and typically variable. Curiously, although we were fairly unrestricted in the colour–magnitude magnitude selection, essentially targeting anything between the main sequence and white dwarf cooling track, J1912–4410 was found in a position very close to AR Sco. This might suggest that a narrow range of orbital and stellar properties, resulting in these observed photometric properties, is required to trigger the pulsed radio emission observed for J1912–4410 and AR Sco. Future searches might benefit from focussing on this region and relaxing or removing infrared criteria.

ACKNOWLEDGEMENTS

IP acknowledges support from the Royal Society through a University Research Fellowship (URF\R1\231496). VSD and ULTRACAM/ULTRASPEC operations are funded by the Science and Technology Facilities Council (grant ST/Z000033/1). GT was supported by grant IN109723 from the *Programa de Apoyo a Proyectos de Investigación e Innovación Tecnológica* (PAPIIT). Part of the data was based on observations made with the GTC telescope, in the Spanish Observatorio del Roque de los Muchachos of the Instituto de Astrofísica de Canarias, under Director’s Discretionary Time. This work was supported by Naresuan University (NU), and National Science Research and Innovation Fund (NSRF), grant no. R2567B015. This work has made use of data obtained at the Thai National Observatory on Doi Inthanon, operated by NARIT. This project has received funding from the European Research Council (ERC) under the European Union’s Horizon 2020 research and innovation programme (grant agreement no. 101020057).

DATA AVAILABILITY

The data analysed in this work can be made available upon reasonable request to the authors.

REFERENCES

- Barrett P., Dieck C., Beasley A. J., Mason P. A., Singh K. P., 2020, *Adv. Space Res.*, 66, 1226
- Barwig H., Ritter H., Barnbantner O., 1994, *A&A*, 288, 204
- Bellm E. C. et al., 2019, *PASP*, 131, 018002
- Bera P., Bhattacharya D., 2018, *MNRAS*, 474, 1629
- Bernardini F., de Martino D., Mukai K., Falanga M., 2014, *MNRAS*, 445, 1403
- Bonnet-Bidaud J. M. et al., 2020, *A&A*, 633, A145
- Bookbinder J. A., Lamb D. Q., 1987, *ApJ*, 323, L131
- Briceño C. et al., 2019, *AJ*, 157, 85
- Cánovas H. et al., 2019, *A&A*, 626, A80
- Cantat-Gaudin T. et al., 2018, *A&A*, 618, A93
- Cantat-Gaudin T. et al., 2020, *A&A*, 640, A1
- Cepa J. et al., 2003, in Iye M., Moorwood A. F. M., eds, Proc. SPIE Conf. Ser. Vol. 4841, Instrument Design and Performance for Optical/Infrared Ground-based Telescopes. SPIE, Bellingham, p. 1739
- Coppejans D. L., Körding E. G., Miller-Jones J. C. A., Rupen M. P., Knigge C., Sivakoff G. R., Groot P. J., 2015, *MNRAS*, 451, 3801
- Cropper M., 1990, *Space Sci. Rev.*, 54, 195
- Cutri R. M. et al., 2021, VizieR Online Data Catalog, II/328
- de Ruiter I. et al., 2025, *Nat. Astron.*, in press. Available at: <https://doi.org/10.1038/s41550-025-02491-0>
- Dhillon V. S. et al., 2007, *MNRAS*, 378, 825
- Dhillon V. S. et al., 2014, *MNRAS*, 444, 4009
- Drake A. J. et al., 2009, *ApJ*, 696, 870
- Drake A. J. et al., 2017, *MNRAS*, 469, 3688
- Feinstein A. D. et al., 2019, *PASP*, 131, 094502
- Ferrario L., Wickramasinghe D. T., Bailey J., Hough J. H., Tuohy I. R., 1992, *MNRAS*, 256, 252
- Ferrario L., Wickramasinghe D., Bailey J., Buckley D., 1995, *MNRAS*, 273, 17
- Fuentes J. R., Cumming A., Castro-Tapia M., Anders E. H., 2023, *ApJ*, 950, 73
- Gagné J. et al., 2015, *ApJS*, 219, 33
- Gaibor Y., Garnavich P. M., Littlefield C., Potter S. B., Buckley D. A. H., 2020, *MNRAS*, 496, 4849
- Geng J.-J., Zhang B., Huang Y.-F., 2016, *ApJ*, 831, L10
- Gentile Fusillo N. P. et al., 2019, *MNRAS*, 482, 4570
- Gentile Fusillo N. P. et al., 2021, *MNRAS*, 508, 3877
- Ginzburg S., Fuller J., Kawka A., Caiazzo I., 2022, *MNRAS*, 514, 4111
- Gordon Y. A. et al., 2020, *Res. Notes Am. Astron. Soc.*, 4, 175
- Gordon Y. A. et al., 2021, *ApJS*, 255, 30
- Großschedl J. E. et al., 2019, *A&A*, 622, A149
- Halpern J. P., Thorstensen J. R., 2015, *AJ*, 150, 170
- Hameury J. M., 2020, *Adv. Space Res.*, 66, 1004
- Harvey P., Merín B., Huard T. L., Rebull L. M., Chapman N., Evans Neal J. I., Myers P. C., 2007, *ApJ*, 663, 1149
- Herbig G. H., 1960, *ApJS*, 4, 337
- Hurley-Walker N. et al., 2024, *ApJ*, 976, L21
- Inight K. et al., 2023, *MNRAS*, 524, 4867
- Isern J., García-Berro E., Külebi B., Lorén-Aguilar P., 2017, *ApJ*, 836, L28
- Joshi A., Pandey J. C., Rawat N., Raj A., Wang W., Singh H. P., 2022, *AJ*, 163, 221
- King A. R., 1989, *MNRAS*, 241, 365
- Kuijpers J., Pringle J. E., 1982, *A&A*, 114, L4
- Kun M., Balog Z., Kenyon S. J., Mamajek E. E., Gutermuth R. A., 2009, *ApJS*, 185, 451
- Lindegren L. et al., 2021, *A&A*, 649, A4
- Luhman K. L., Esplin T. L., 2020, *AJ*, 160, 44
- Luhman K. L., Herrmann K. A., Mamajek E. E., Esplin T. L., Pecaut M. J., 2018, *AJ*, 156, 76
- Lyo A. R., Lawson W. A., Bessell M. S., 2008, *MNRAS*, 389, 1461
- Mainzer A. et al., 2011, *ApJ*, 731, 53
- Marsh T. R., 1989, *PASP*, 101, 1032
- Marsh T. R. et al., 2016, *Nature*, 537, 374
- Marton G. et al., 2019, *MNRAS*, 487, 2522
- Mason K. O., Middleditch J., Cordova F. A., Jensen K. A., Reichert G., Murdin P. G., Clark D., Bowyer S., 1983, *ApJ*, 264, 575
- Mason E., Wickramasinghe D., Howell S. B., Szkody P., 2007, *A&A*, 467, 277
- Mouchet M. et al., 2017, *A&A*, 600, A53
- Oliveira I. et al., 2009, *ApJ*, 691, 672
- Pala A. F. et al., 2020, *MNRAS*, 494, 3799
- Patterson J., 1994, *PASP*, 106, 209
- Patterson J., Williams G., Hiltner W. A., 1981, *ApJ*, 245, 618
- Pelisolì I., Vos J., 2019, *MNRAS*, 488, 2892
- Pelisolì I. et al., 2022, *MNRAS*, 516, 5052
- Pelisolì I. et al., 2023, *Nat. Astron.*, 7, 931
- Pelisolì I. et al., 2024a, *MNRAS*, 527, 3826
- Pelisolì I. et al., 2024b, *MNRAS*, 531, 1805
- Petrosky E., Hwang H.-C., Zakamska N. L., Chandra V., Hill M. J., 2021, *MNRAS*, 503, 3975
- Pettersson B., Armond T., Reipurth B., 2014, *A&A*, 570, A30
- Potter S. B., Buckley D. A. H., 2018, *MNRAS*, 481, 2384
- Potter S. B. et al., 2010, *MNRAS*, 402, 1161
- Pretorius M. L. et al., 2021, *MNRAS*, 503, 3692
- Reinsch K., Burwitz V., Beuermann K., Schwöpe A. D., Thomas H. C., 1994, *A&A*, 291, L27
- Remillard R. A., Stroozas B. A., Tapia S., Silber A., 1991, *ApJ*, 379, 715
- Ricker G. R. et al., 2015, *J. Astron. Telesc. Instrum. Syst.*, 1, 014003
- Ridder M. E., Heinke C. O., Sivakoff G. R., Hughes A. K., 2023, *MNRAS*, 519, 5922
- Rodríguez A. C., 2025, *A&A*, 695, L8
- Satyvaldiev V., 1971, *Astronomicheskij Tsirkulyar*, 633, 7
- Schreiber M. R., Belloni D., Gänsicke B. T., Parsons S. G., Zorotovic M., 2021, *Nat. Astron.*, 5, 648
- Schreiber M. R., Belloni D., Schwöpe A. D., 2024, *A&A*, 682, L7
- Schwöpe A. D., Mengel S., 1997, *Astron. Nachr.*, 318, 25
- Schwöpe A. D., Thinius B., 2012, *Astron. Nachr.*, 333, 717
- Schwöpe A., Buckley D. A. H., Malyali A., Potter S., König O., Arcodia R., Gromadzki M., Rau A., 2022, *A&A*, 661, A43
- Schwöpe A., Marsh T. R., Standke A., Pelisolì I., Potter S., Buckley D., Munday J., Dhillon V., 2023, *A&A*, 674, L9
- Silber A. D., Remillard R. A., Horne K., Bradt H. V., 1994, *ApJ*, 424, 955
- Spina L. et al., 2021, *MNRAS*, 503, 3279
- Stanway E. R., Marsh T. R., Chote P., Gänsicke B. T., Steeghs D., Wheatley P. J., 2018, *A&A*, 611, A66
- Stiller R. A., Littlefield C., Garnavich P., Wood C., Hamsch F.-J., Myers G., 2018, *AJ*, 156, 150
- Takata J., Hu C. P., Lin L. C. C., Tam P. H. T., Pal P. S., Hui C. Y., Kong A. K. H., Cheng K. S., 2018, *ApJ*, 853, 106
- Tapia S., 1977, *IAU Circ.*, 3054, 1
- Thorstensen J. R., Halpern J. P., 2009, *Astron. Telegram*, 2177, 1
- Thorstensen J. R., Lépine S., Shara M., 2006, *PASP*, 118, 1238
- Thorstensen J. R., Alper E. H., Weil K. E., 2016, *AJ*, 152, 226
- Thorstensen J. R., Motsoaledi M., Woudt P. A., Buckley D. A. H., Warner B., 2020, *AJ*, 160, 70
- Tonry J. L. et al., 2018, *PASP*, 130, 064505
- Tovmassian G. H., Greiner J., Zickgraf F. J., Kroll P., Krautter J., Thiering I., Zharykov S. V., Serrano A., 1997, *A&A*, 328, 571
- van Eyken J. C. et al., 2011, *AJ*, 142, 60
- VanderPlas J. T., Ivezić Ž., 2015, *ApJ*, 812, 18
- Vanderplas J., 2015, gatspy: General tools for Astronomical Time Series in Python. Zenodo. Available at: <https://doi.org/10.5281/zenodo.14833>
- Visvanathan N., Pickles A., 1982, *Nature*, 298, 41
- Voikhanskaya N. F., 1987, *Sov. Astron. Lett.*, 13, 250
- Walker M. F., 1965, *Commun. Konkoly Observatory Hungary*, 57, 1
- Wilson A. J., Lakeland B. S., Wilson T. J., Naylor T., 2023, *MNRAS*, 521, 354
- Wright E. L. et al., 2010, *AJ*, 140, 1868

APPENDIX: PREVIOUSLY KNOWN SYSTEMS

A1 Polars

V* BL Hyi: a well-studied polar with a period of 100 min (e.g. Visvanathan & Pickles 1982).

CRTS J035758.7+102943: a polar with a period of 1.900344(24) h (Schwope & Thinius 2012; Thorstensen, Alper & Weil 2016).

V* UW Pic: a known polar with an orbital period of 2.225 h and a magnetic field strength of 19 MG (Reinsch et al. 1994).

PPMXL 3189652360374206258: classified as a polar by Halpern & Thorstensen (2015), who report a period of 1.70177(26) h.

V* HS Cam: known eclipsing polar with a period of 1.637 h (Tovmassian et al. 1997).

V* VV Pup: a polar (Tapia 1977) showing QPOs (Bonnet-Bidaud et al. 2020). It has an orbital period of 1.67 h (Walker 1965) and a magnetic field structure that is well described by a 40 MG offset dipole (Mason et al. 2007).

V* V834 Cen: a well-known polar showing QPOs (Mouchet et al. 2017). The orbital period is 1.692 h (Mason et al. 1983) and it has a magnetic field of 23 MG (Ferrario et al. 1992).

2MASS J14534105–5521387: this is a polar showing QPOs. Its orbital period is 3.1564(1) h, and it was characterized by Potter et al. (2010).

V* V2301 Oph: a well-characterized eclipsing polar also known as H 1752+081. The orbital period is 1.882801 h (Barwig, Ritter & Barnbantner 1994; Silber et al. 1994). It has a relatively low magnetic field strength for a polar, of 7 MG (Ferrario et al. 1995).

V* EP Dra: also known as H 1907+690, this is a well-characterized eclipsing polar. The reported orbital period is 1.743750 h (Remillard et al. 1991), and the magnetic field strength is 16 MG (Schwope & Mengel 1997).

2MASS J19293303–5603434: an eclipsing polar with an orbital period of 92.5094 ± 0.0002 min recently discovered by Schwope et al. (2022).

Gaia DR2 1956566510538468224: there was a *Gaia* alert for these system, Gaia18aya. It was followed-up by Thorstensen et al. (2020) who identified it as a polar with magnetic field strength of ~ 50 MG and orbital period of $2.002757(38) \pm$ h.

RX J2218.5+1925: also known as Swift J2218.4+1925, this is a known polar with an orbital period of 2.158 ± 0.003 h. It was initially classified from optical spectroscopy by Thorstensen & Halpern (2009), and further characterized from X-ray data by Bernardini et al. (2014).

A2 Intermediate polar

PPMXL 2431202680279124324: an intermediate polar with a spin period of 1412 s and orbital period of 81 min (Halpern & Thorstensen 2015).

A3 Young stellar objects

SSS J035055.8–204817: Pala et al. (2020) obtained spectra of this object and concluded it to be a YSO due to the presence of lithium and of forbidden lines of [O I] (5577 and 6300 Å) and [S II] (6730 Å), commonly observed for YSOs but not CVs.

2MASS J05301240+0148214: a T Tauri star in the Orion OB1 association (Briceño et al. 2019).

2MASS J05315396+0242310: reported as a likely classical T-Tauri star by van Eyken et al. (2011).

2MASS J05371640–0711463: a YSO in the Orion A molecular cloud (Großschedl et al. 2019).

Gaia DR2 3336335474617325568: a member of the Collinder 69 open cluster (Cantat-Gaudin et al. 2018), which is ≈ 12 Myr old (Cantat-Gaudin et al. 2020).

2MASS J05422602–0308566 and 2MASS J05405519–0247497: H α emission-line stars in a molecular cloud towards the M42 open cluster (Pettersson, Armond & Reipurth 2014).

Gaia DR2 5329108769930689664: is a member of the open cluster IC 2395 (Cantat-Gaudin et al. 2018), which is ≈ 20 Myr old (Cantat-Gaudin et al. 2020).

[FLG2003] eps Cha 11: this a pre-main sequence star in the η Chamaeleontis cluster that is viewed through an edge-on disc (Lyo, Lawson & Bessell 2008).

BPS CS 30311–0012: this is classified as a young (sub)stellar object by Gagné et al. (2015).

CRTS J155929.1–223618 and EPIC 204388640: these are young stars in the direction, and possible members, of the Upper Scorpius association (Luhman & Esplin 2020).

2MASS J16063093–2258150: this object has been spectroscopic classified as a galaxy by Luhman et al. (2018), which would require its *Gaia* parallax of 7.270 ± 0.220 mas to be very inaccurate. More recently, relying on *Gaia* data, it was classified as a candidate member of the Upper Scorpius association (Luhman & Esplin 2020).

Gaia DR2 6048855674228736128: has been identified as a candidate member of the association ρ Ophiuchi by Cánovas et al. (2019).

2MASS J18294021+0015127: a well-characterized YSO in the Serpens association (Harvey et al. 2007; Oliveira et al. 2009).

2MASS J21205785+6848183: this is a pre-main sequence star that is part of the G109+11 association, as determined by Kun et al. (2009). They remark that the precise nature of the system is uncertain, with observed properties being consistent with an edge-on disc or an unresolved binary.

This paper has been typeset from a $\text{\TeX}/\text{\LaTeX}$ file prepared by the author.